Nature Geosciences article

Constraints on the shallow elastic and anelastic structure of Mars from InSight seismic data

List of authors

P.Lognonné[1,35], W.B. Banerdt[2], W.T.Pike[3], D.Giardini[4], U.Christensen[5], R.F.Garcia[6],T.Kawamura[1], S.Kedar[2], B. Knapmeyer-Endrun[7], L.Margerin[8], F.Nimmo[9], M.Panning[2], B.Tauzin[10], J.-R.Scholz[5], D.Antonangeli[11], S.Barkaoui[1], E.Beucler[12], F. Bissig[4], N. Brinkman[4], M. Calvet[8], S,Ceylan[4] C.Charalambous[3], P.Davis[13], M. van Driel[4], M.Drilleau[1], L.Fayon[14], R. Joshi[5], B.Kenda[1], A. Khan[4,36], M. Knapmeyer[15], V. Lekic[16], J.McClean[3], D.Mimoun[6], N.Murdoch[6], L. Pan[10], C.Perrin[1], B.Pinot[6], L.Pou[9] , S. Menina[1], S.Rodriguez[1,35] , C. Schmelzbach[4], N. Schmerr[16], D. Sollberger[4], A.Spiga[17,35], S.Stähler[4], A.Stott[3], E.Stutzmann[1], S.Tharimena[2], R.Widmer-Schnidrig[18], F. Andersson[4], V.Ansan[12], C. Beghein[13], M.Böse[4],E. Bozdag[19], J. Clinton[4], I.Daubar[2], P.Delage[20], N. Fuji[1], M. Golombek[2], M. Grott[15], A. Horleston[21], K. Hurst[2], J. Irving[22], A. Jacob[1], J. Knollenberg[15], S.Krasner[2], C. Krause[15], R. Lorenz[23], C. Michaut[24,35], B.Myhill[21], T. Nissen-Meyer[25], J. ten Pierick[4], A.-C..Plesa[15], C.Quantin-Nataf[10], J.Robertsson[4], L. Rochas[26], M.Schimmel[27], S.Smrekar[2], T.Spohn[15], N.Teanby[21], J.Tromp[22], J.Vallade[26] , N.Verdier[26], C.Vrettos[28], R. Weber[29], D.Banfield[30], E. Barrett[2], M.Bierwirth[5], S.Calcutt[31], N.Compaire[6], C.Johnson[32,37], D.Mance[4], F. Euchner[4], L.Kerjean[26], G.Mainsant[6], A.Mocquet[12],J.Antonio Rodriguez Manfredi[33], G.Pont[26], P.Laudet[26], T.Nebut[1], S. de Raucourt[1], O. Robert[1], C.T. Russell[13], A.Sylvestre-Baron[26], S.Tillier[1], T.Warren[3], M.Wieczorek[34], C.Yana[26], P.Zweifel[4]

Affiliations:

(1) Université de Paris, Institut de physique du globe de Paris, CNRS, F-75005 Paris, France
(2) Jet Propulsion Laboratory, California Institute of Technology, Pasadena, CA 91109, USA
(3) Department of Electrical and Electronic Engineering, Imperial College London, South Kensington Campus, London SW7 2AZ, UK
(4) Institute of Geophysics, ETH Zurich, Sonneggstr. 5, 8092 Zurich, Switzerland
(5) Max Planck Institute for Solar System Research, Justus-von-Liebig-Weg 3, 37077 Göttingen, Germany
(6) Institut Supérieur de l'Aéronautique et de l'Espace SUPAERO, 10 Avenue Edouard Belin, 31400 Toulouse, France
(7) Bensberg Observatory, University of Cologne, Vinzenz-Pallotti-Str. 26, 51429 Bergisch Gladbach, Germany
(8) Institut de Recherche en Astrophysique et Planétologie, Université Toulouse III Paul Sabatier, CNRS, CNES, 14 Av. E. Belin, 31400, Toulouse, France
(9) Dept. of Earth and Planetary Sciences, University of California Santa Cruz, Santa Cruz, CA 95064, USA
(10) Université de Lyon, Université Claude Bernard Lyon 1, ENS, CNRS, Laboratoire de Géologie de Lyon : Terre, Planètes, Environnement, 69622 Villeurbanne, France
(11) Sorbonne Université, Muséum National d'Histoire Naturelle, UMR CNRS 7590, Institut de Minéralogie, de Physique des Matériaux et de Cosmochimie, IMPMC, 75005 Paris, France
(12) Laboratoire de Planétologie et Géodynamique, UMR6112, Univ. Nantes, Univ. Angers, CNRS, 2 rue de la Houssinière - BP 92208, 44322 Nantes Cedex 3, France
(13) Department of Earth, Planetary, and Space Sciences, University of California Los Angeles, CA90095, USA
(14) Space Exploration Institute, Neuchâtel, Switzerland
(15) DLR Institute of Planetary Research, Rutherfordstr. 2, 12489 Berlin, Germany
(16) University of Maryland, College Park, Department of Geology, 8000 Regents Dr., College Park, MD, 20782-4211, USA
(17) Laboratoire de Météorologie Dynamique / Institut Pierre Simon Laplace (LMD/IPSL), Sorbonne Université, Centre National de la Recherche Scientifique (CNRS), École Polytechnique, École Normale Supérieure (ENS), Campus Pierre et Marie Curie BP99, 4 place Jussieu, 75005 Paris, France
(18) Black Forest Observatory, Stuttgart University, Heubach 206, D-77709 Wolfach, Germany
(19) 1500 Illinois Street, Colorado School of Mines, Department of Geophysics, Golden, 80401 CO, USA
(20) Laboratoire Navier/CERMES, CNRS, 6-8 av. B. Pascal, F 77455 Marne la Vallée cedex 2, France
(21) School of Earth Sciences, University of Bristol, Wills Memorial Building, Queens Road, Bristol BS8 1RJ, UK
(22) Department of Geosciences, Princeton University, Princeton, NJ, 08544, USA
(23) Johns Hopkins Applied Physics Laboratory, 11100 Johns Hopkins Road, Laurel, MD 20723, USA
(24) Université de Lyon, École Normale Supérieure de Lyon, UCBL, CNRS, Laboratoire de Géologie de Lyon - Terre, Planètes, Environnement, 69007 Lyon, France
(25) Department of Earth Sciences, University of Oxford, South Parks Road, Oxford OX1 3AN, United Kingdom
(26) Centre Nationale d'Etudes Spatiale, 18 avenue Edouard Belin, 31401 Toulouse Cedex 9, France
(27) Institut of Earth Science Jaume Almera (ICTJA), 08028, Barcelona, Spain
(28) Division of Soil Mechanics and Foundation Engineering, Technical University of Kaiserslautern, 67663 Kaiserslautern, Germany
(29) NASA MSFC, NSSTC Mail Code ST13, 320 Sparkman Drive, Huntsville, AL 35805, USA
(30) Cornell Center for Astrophysics and Planetary Science, Cornell University, Ithaca, USA
(31) University of Oxford, Department of Physics, Parks Road, Oxford OX1 3PU, UK
(32) Deptartment of Earth, Ocean and Atmospheric Sciences, University of British Columbia, Vancouver, BC, V6T 1Z4, Canada
(33) Centro de Astrobiologia - Instituto Nacional de Tecnica Aeroespacial, Spain
(34) Université Côte d'Azur, Observatoire de la Côte d'Azur, CNRS, Laboratoire Lagrange, France
(35) Institut Universitaire de France, 1 rue Descartes, 75005 Paris, France
(36) Institute of Theoretical Physics, University of Zürich, Zürich, Switzerland
(37) Planetary Science Institute, Tucson, AZ 85719, USA

Abstract :

Mars's seismic activity and noise have been monitored since January 2019 by the seismometer of the InSight (Interior exploration using Seismic Investigations, Geodesy and Heat Transport) lander. At night, Mars is extremely quiet; seismic noise is about 500 times lower than Earth's micro-seismic noise at periods between 4 and 30 seconds. The recorded seismic noise increases during the day, due to ground deformations induced by convective atmospheric vortices and ground-transferred wind-generated lander noise. Here we constrain properties of the crust beneath InSight, using signals from atmospheric vortices and from the hammering of InSight's Heat Flow and Physical Properties (HP^3) instrument, as well as the three largest Marsquakes detected as of September 2019. From receiver function analysis, we infer that the uppermost 8 to 11 km of the crust is highly altered and/or fractured. We measure the crustal diffusivity and intrinsic attenuation using multi-scattering analysis, and find that seismic attenuation is about 3 times larger than on the Moon, which suggests that the crust contains small amounts of volatiles.

Main Text

The Interior Exploration using Seismic Investigations, Geodesy and Heat Transport (InSight) mission landed on Mars on November, 26th, 2018 in Elysium Planitia[1,2], 38 years after the end of Viking 2 lander operations. At the time, Viking's seismometer[3] did not succeed in making any convincing Marsquake detections, due to its on-deck installation and high wind sensitivity[4]. InSight therefore provides the first direct geophysical in-situ investigations of Mars' interior structure by seismology[1,4].

Seismic Experiment for Interior Structure (SEIS)[5] monitors the ground acceleration with 6 axes: 3 Very Broad Band (VBB) oblique axes, sensitive to frequencies from tidal up to 10 Hz, and one vertical and two horizontal Short Period (SP) axes, covering frequencies from ~ 0.1Hz up to 50 Hz. SEIS is complemented by the APSS experiment[6] (InSight Auxiliary Payload Suite), which includes pressure, TWINS[7] (Temperature and Winds for InSight) sensors and a magnetometer. These sensors monitor the atmospheric sources of seismic noise and signals.

After seven sols (Martian days) of SP on-deck operation, with seismic noise comparable to Viking[3], InSight's robotic arm[8] placed SEIS on ground twenty-two sols after landing, at a location selected through analysis of InSight's imaging data[9]. After leveling and noise assessment, the Wind and Thermal Shield (WTS) was deployed on Sol 66 (February, 2, 2019). A few days later, all 6 axes started continuous seismic recording, at 20 sample per second (sps) for VBBs and 100 sps for SPs. After onboard decimation, continuous records at rates from 2 to 20 samples per seconds (sps) and event records[5] at 100sps are transmitted.

Several layers of thermal protection and very low self-noise enable the SEIS VBB sensors to record the daily variation of the seismic noise at Mars' surface, down to the lowest noise recorded so far by a seismometer on the surface of a terrestrial body, at periods between 5 and 20 seconds.

Figure 1 shows the spectrogram of a typical sol of seismic data on Mars (sol 194-195), in the 0.1-50 Hz band. Starting at 17:00-18:00 LMST (Local Mean Solar Time), extremely low noise levels are observed until midnight. During the lowest wind period, accelerations below 1.5 10^{-10} $m/s^2/Hz^{1/2}$ at 0.4 Hz are detected, corresponding to ~3 Å RMS ground displacement in a one-octave bandwidth. This is ~1/500 of the Earth Low Noise Model[10] (LNM), allowing detection of events with a moment magnitude M_w ~1.8 lower than on Earth. The levels of noise are comparable to those recorded by Apollo[11] on the Moon at 1 Hz ***(Figure 2***), but much lower at longer periods. After midnight, the noise increases slightly until sunrise, and then rises rapidly with atmospheric boundary layer activity, from 7:00-16:00 LMST, still remaining below the LNM between 2 and 20 seconds. These three noise regimes, associated with wind ranging from night-time laminar flow to daily turbulent flow will likely provide new constraints on the Martian Planetary Boundary layer[13] when better understood.

Correlation analyses of SEIS with pressure and wind data (***Supplement 1***) confirm the Martian environment as the key contributor to seismic noise, in line with pre-landing predictions[14-19]. Observations (***Figure S1-3 to S1-4 of Supplement 1)*** suggest that long periods are dominated by ground deformation due to pressure perturbation and wind stresses while shorter periods are dominated by lander-generated noise excited by wind.

Subsurface constraints from atmospheric vortices and HP3

The elastic properties of Mars' near-surface (upper 10-20m) provide information on geological processes that have shaped the landing site but are also required to fully understand the seismic noise. We derive a first elastic model using three independent seismic techniques at vertical scales varying from a few centimeters to ~10 meters and at horizontal scales up to several tens of meters.

At a 5-cm scale, SEIS's feet with their 2 cm spikes are in contact with the duricrust, a thin, weakly cemented layer about 1cm below unconsolidated soil[3]. From the modeling of resonant frequencies of the SEIS leveling system[20], a local Young's modulus of 47 MPa is inferred ***(Supplement 2-1)***. This value is in agreement with geological inferences of a cohesive layer about 35% stiffer than the material immediately below[3].

At a 1-m scale, the bulk seismic velocity of the regolith was constrained using travel-time measurements of hammer strokes from HP^3 hammering[21], acting as a seismic source at 0.33 m depth. See method[22-23] and ***Supplement 2-2*** for details. Through precise knowledge of the HP^3

and SEIS clocks and averaging data from multiple hammer strokes, the travel time was determined to be 9.40 ± 2.68 ms over a distance of 1.11m, yielding an apparent P-wave velocity estimate of V^{app}_{P}=120 ± 40m/s.

At horizontal scales of 10-100 meters (Figure S2-5), the near-surface material was probed using ground deformation caused by convective vortices ***(Supplement 2-3)***, or 'dust devils' if made visible by their dust content, passing in the vicinity of InSight and producing distinct pressure drops detected by APSS[7], as well as vertical motion and ground tilt, detected by SEIS (***Figure 3***). The ground velocity and pressure measurements[24-25] provide values for the ground compliance, computed as the ratio of the signal's ground velocity to its correlated atmospheric pressure. Compliance is a function of wavelength, and thus can provide depth-dependent elastic properties of the subsurface[16-17, 24-25].

V^{app}_{p} and the ground compliance provide complementary constraints on properties of the upper regolith layer and the brecciated bedrock beneath. Figure 4 presents the probability density function (PDF) of possible seismic structures of the topmost 10 m using these constraints and assuming a near-surface compaction model[26]. The most probable models are generally consistent with the regional geological structure[3], with V_P ranging from 90 m/s ~5 cm below the surface to 145 m/s at ~80 cm depth. This suggests that the degraded crater (Homestead Hollow) where SEIS is deployed is filled largely with unconsolidated cohesionless sandy material[3] with seismic velocities lower than those of previously considered Mars analogues[27]. A compliance-only inversion (Figure S2-6) provides larger probabilities for stiffer regolith, but samples a larger surface area.

Crustal seismic attenuation and diffraction

This first seismic structural analysis of Mars is based on the three best-recorded quakes until 9/2019, occurred on sol 128, 173 and 235. Their amplitudes exceed 10^{-8} $m/s^2/Hz^{1/2}$ either below 1 Hz (S0173a and S0235b) or above 1Hz (S0128a). The complete collection of seismic sources includes 171 other events[4, 28] with smaller amplitudes.

The peak-to-peak vertical ground acceleration of S0128a is about 8.5 10^{-7} m/s^2 in the 2-10 Hz bandwidth (Figure S1-9). Those of S0173a and S0235b are 3.5 10^{-8} m/s^2 and 3.5 10^{-8} m/s^2 respectively in the 0.2-1 Hz bandwidth (Fig. S1-10/11). None have surface waves suggesting a depth too large to excite them above the noise and/or surface waves scattering[4]. Their high Signal to Noise Ratio (SNR), particularly with respect to wind (***Supplement 1*** and corresponding spectra, seismograms and wind/pressure records in Fig. S1-8 to S1-11) enable us to (i) characterize attenuation and diffraction in the Martian crust and (ii) search for upper-crustal layering using the receiver function method to identify conversion of seismic waves during their propagation in the crust.

All three large events are dominated by long incoherent wavetrains. Polarization analysis reveals a high degree of polarization for only a small fraction of the time. Scattering is a possible candidate to explain some of the signal characteristics. Scattering and attenuation properties are estimated from the S0128a, S0173a and S0235b records.

S0128a signal is above the noise floor for frequencies >2.5 Hz. The morphology of its seismogram is very similar to those of Moonquakes[29] as illustrated in Figure 5 (right). The waveform is characterized by a stabilization of the ratio between the kinetic energies measured on the vertical (V) and horizontal (H) components, which is very reminiscent of high-frequency coda waves excited by small crustal quakes on Earth[30]. Further examination, described in **Supplement 3** reveals two energy bursts, the first one being mostly visible above 6Hz. Due to the lack of polarization, one cannot confidently identify the first burst as P and the second one as S. However, a simplified elastic radiative transfer calculation reproduces reasonably well the two energy packets seen in the data for a hypocentral distance Δ=530 km, v_s=3 km/s and a poissonian v_p/v_s. Furthermore, the model shows that the signal between the tentative P and S arrivals is largely dominated by S waves which offers an attractive explanation for the stabilization of the vertical to horizontal energy partitioning ratio during the event. The absorption time of shear waves (~80-85 sec) yields an absorption quality factor Q_i ~ 3770—4006 at 7.5Hz. In the event frequency band, the decay time appears rather constant so that we may speculate that Q_i~503—534 at 1Hz. The diffusivity inferred from the data (D~90 km^2/s) depends strongly on the hypocentral distance, which is poorly determined. For instance with a distance of 375km (found for t_s-t_p = 75s, V_s=2.5 km/s and V_p/V_s=2 where t_s and t_p are the arrival times of P and S), the diffusivity is reduced by a factor of 2. But whereas the inferred diffusivity is strongly dependent on the assumed quake location, the absorption time is not. Note however, that only an apparent absorption has been derived since the possible leakage of diffuse energy from crust to mantle has been neglected[31].

Further constraints on attenuation have been gained through the analysis of S0173a and S0235b events. Both events contain signal above the noise floor between 0.2-0.9 Hz and shows identifiable, coherent P and S pulses with approximately linear polarization. After each coherent arrival, the signal shows a coda with no characteristic polarization. The SNRs are higher than for S0128a and the events are located at roughly 1720 km and 1535km distance[4]. This suggests seismic waves propagating in a relatively transparent but attenuating Martian mantle before entering the regional crustal structure beneath InSight.

The observed long coda duration appears to be due to the interaction of teleseismic waves with a heterogeneous crust. Using a simple acoustic radiative transfer model in a waveguide geometry, we inverted for D and the intrinsic attenuation factor Q_i for S waves in the crust, based on the coherent S wave and its coda (see **Supplement 3**). In spite of its simplicity the model takes leakage into account which is key to obtain a reliable estimate of absorption. The trade-off[32] between D and Q_i is studied in Supplement 3. Our analysis suggests a diffusivity $D \geq 200$ km^2/s and a quality factor $Q_i \geq 800$ at 0.5 Hz. The later bound is roughly 3 times lower than reported for the dry megaregolith of the Moon in the same frequency band[33].

Thanks to these three events, preliminary comparisons with the scattering and attenuation properties of the shallow part of the Earth and Moon can be made. The diffusivity of Mars ranges from 40 km^2/s (from S0128a) to 600 km^2/s (from S0173a and S0235b). The gap in diffusivity between regional and teleseismic events may in large part be related to the difference in frequencies, as diffusivity generally decreases with increasing frequency. Estimates of absorption are obtained from the two teleseismic events which both suggests Q_i ~800, possibly higher. The coda quality factor of S0128a (518±16) can be reconciled by remembering that energy leakage has been neglected in the Q_i estimation of this event.

Figure 5 shows typical estimates of D and Q_i on Earth, Moon and Mars. Earth values are at 1.5 Hz and scattering quality factors reported in literature have been converted to diffusivity assuming an average crustal shear crustal velocity of 3km/s. For Earth, we show the range of propagation properties due to variability of the geological environment, which is directly reflected in the waveforms. The low-attenuation, weakly scattering crust of old crystalline massifs shows clear ballistic phases including mantle head waves up to large distances and long-lasting codas where multiple reverberations play an important role. In sharp contrast, in volcanic areas the medium is strongly scattering and attenuating, coherent phases are absent and the propagation is predominantly diffusive. The Moon displays strong scattering like terrestrial volcanic areas with very little or virtually no dissipation, due to the low volatile content of the crust. Dissipation on Mars appears intermediate between Earth and the Moon, comparable to those of crystalline massifs: relatively low compared to tectonic areas on Earth[32], but much stronger than on the Moon. Scattering also has intermediate values between the Moon and terrestrial crystalline massifs. The relatively moderate scattering may in fact reflect additional complexities of the medium, in particular the stratification of subsurface materials, which remains to be explored.

Upper crustal layering from receiver function modeling

Crustal structure beneath the landing site can be investigated at depths larger than a few tens of meters using receiver-side converted S-waves within the teleseismic P-wave coda. These conversions are generated when an incident planar P-wave encounters a discontinuity in the subsurface (Fig. 6a). The relative arrival times of these converted phases are dependent on the depth of the discontinuity and seismic wave velocities above it, whereas their amplitudes are related to the impedance contrast at the discontinuity. Positive amplitudes indicate a velocity increase with depth at the discontinuity.

The converted phases can be extracted from seismograms by deconvolving the incoming P wavetrain on the vertical component from the radial component, which minimizes complexity due to source effects and propagation through Mars' interior. Individual arrivals associated with sub-receiver conversions can then be readily identified in the resulting P-to-s receiver function (RF).

Over the past 40 years, RFs have become a standard method to study crustal and upper-mantle structure of the Earth[34-35] and have also been applied to lunar seismic data[36-37]. See ***Supplement 4*** and Supplementary Figures S4-2 to S4-4 for the specific methodology used.

We focus on the early part of P-to-s RFs (0-5sec) of S0173a and S0235b which is related to crustal structure[38]. Both events have distinct seismic arrivals and their epicenters are ~450 km apart, at ~26°-28° epicentral distance[4]. A broad-band "glitch" contaminates the VBB seismograms of S0173a about 15 s after the P-onset (Figure S1-9), requiring glitch removal (***Supplement 5***).

Fig. 6b, c show RFs obtained for several deglitching algorithms and RF methods. See ***Supplement 4*** for details. The variability between individual results provides an estimate of the single-event receiver function uncertainty. An alternative estimate can be obtained by applying transdimensional hierarchical Bayesian (THB) deconvolution[39], which yields an ensemble of RFs compatible with the data (Fig. 6c). An initial positive arrival is consistently observed for all methods at 2.2-2.4 s, followed by a second positive arrival 4.6-4.7 s after the P-wave. The later part of the receiver functions shows higher variability among different methods.

The same two phases are also observed in the RFs for the glitch-free S0235b event. As these two quakes are located in different directions from InSight (91^{o} back-azimuth for S0173a vs. 74^{o} for S0235b), this suggests that the phases are caused by crustal layering beneath the receiver rather than distributed scatterers along their propagation paths. Clear multiple converted and reflected phases could not yet be unambiguously identified within these data. The peak at 2.2-2.4 s indicates a discontinuous velocity increase between 8 to 11 km depth and an S-wave velocity 1.7-2.1 km/s within the topmost layer (see ***Supplement 4*** and Figure S4-9). The nearly constant relative timing between the peaks at 2.2-2.4 and 4.6-4.7sec and a phase around 7 s observed in some of the different realizations of the RF could indicate that these phases are reverberations generated at the same velocity contrast with comparable travel time for each additional reflection. However, the absence of any unambiguous accompanying negative arrivals and the comparatively large apparent P-wave incidence angles of more than 25° as derived from various polarization measurements (see ***Supplementary Figure S4-8***) argue against reverberations in a near-surface low-velocity layer (***Supplementary Figures S4-6, S4-7***) and are more compatible with structure at depth causing the later arrivals.

No signals before 2.2 s, including oscillating waveforms as expected for a shallow strong impedance contrast, are found. The regolith layer is therefore not resolved by the receiver functions and must be thinner than a few tens of meters (see ***Supplement 4 and Figures S4-5***), in agreement with our compliance analysis. The transverse components of the RFs are at the noise level of the vertical components; thus we have no evidence for crustal anisotropy (***Supplementary Figure S4-5***).

First seismic constraints on the Martian crust

Even though large quakes with multiple surface wave arrivals[41, 43-44] or located impacts[45] have not yet been detected, SEIS already constrains the Martian crust and utilizes a new source of seismic information through the interaction of the Martian atmosphere with ground.

SEIS data confirm, with both compliance and RFs, a thin (few meters) regolith layer over a more competent layer in the vicinity of the lander. Much deeper, a crustal layer with S-wave velocity between 1.7 and 2.1 km/s extending down to 8 and 11 km depth is suggested by the first SEIS RF analysis. Gamma-Ray Spectrometer chemical mapping[46] and geology[47] suggest that the uppermost crustal layers are composed of basaltic rocks. Reduced velocities by up to 50% with respect to Earth's analogs (Table S4-1) imply therefore highly altered and/or damaged layers[48].

Finally, the attenuations inferred from S0128a, S0173a and S0235b are significantly higher than in the lunar crust and is suggesting a crust with small amounts of volatiles[49]. As diffusivity and thickness of the crust remain weakly constrained, we cannot entirely reject the possibility that these attenuations reflect energy leakage. However, inversions of S0173a and S0235b data indicate that absorption may well be the dominant process and is comparable to Earth's crystalline massifs. The Q_i from S0173a and S0235b signals agrees with lithospheric Q_i proposed pre-launch[48]. Further work will be needed to confirm this interpretation and to delineate more precisely the stratification of attenuation in Mars crust and lithosphere.

Additional locatable events, especially at larger epicentral distances, and complementary methods (e.g., noise autocorrelations) will reduce uncertainties and will provide tighter constraints on the elastic and anelastic structure, including depth of the crust/mantle discontinuity. Events with $M_w > 4.5$ will ultimately provide deep interior's constraints[5,41].

References :

[1] Banerdt, W. B. et al. The InSight mission. *Nature geosciences*, submitted (2019).

[2] Golombek, M. et al. Geology of the InSight landing Site, Mars. *Nature Communication*, submitted (2019).

[3] Anderson, D.L. Seismology on Mars, *J. Geophys. Res.* **82**, 4524-4546, http://doi.org/10.1029/JS082i028p04524 (1977).

[4] Giardini, D. et al. The seismicity of Mars. *Nature geosciences*, submitted (2019).

[5] Lognonné, P.et al., SEIS: Insight's Seismic Experiment for Internal Structure of Mars. *Space Sci. Rev.* **215,** 12, http://doi.org/10.1007/s11214-018-0574-6 (2019).

[6] Banfield, D. et al.InSight Auxiliary Payload Sensor Suite (APSS). *Space Sci. Rev.* **215,** 4, http://doi.org/10.1007/s11214-018-0570-x (2019).

[7] Banfield, D.et al. An overview of the initial results on atmospheric science from InSight measurements. *Nature Geosciences*, submitted (2019).

[8] Trebi-Ollennu, A.et al. InSight Mars lander robotics instrument deployment system. *Space Sci. Rev.* **214,** 93, http://doi.org/10.1007/s11214-018-0520-7 ,(2018).

[9] Maki, J. N. et al. The color cameras on the InSight lander, *Space Sci. Rev.* **214,** 105, http://doi.org/10.1007/s11214-018-0536-z (2018).

[10] Peterson J., Observations and modelling of background seismic noise. Open-file report 93-322, U.S. Geological Survey, Albuquerque, New Mexico. http://earthquake.usgs.gov.regional/asl/pubs/ (1993).

[11] Lognonné, P. & Johnson, C. L. 10.03 - Planetary Seismology, Editor(s): Gerald Schubert, *Treatise on Geophysics* (Second Edition), 65-120 (Elsevier, 2015), https://doi.org/10.1016/B978-0-444-53802-4.00167-6.

[12] Clinton, J. et al. The Marsquake Service: Securing Daily Analysis of SEIS Data and Building the Martian Seismicity Catalogue for InSight. *Space Sci. Rev.* **214,** 133. https://doi.org/10.1007/s11214-018-0567-5 (2018).

[13] Spiga, A. Atmospheric Science with InSight. *Space Sci. Rev.*, **214,** 109. http://doi.org/10.1007/s11214-018-0543-0 (2019).

[14] Lognonné P. & Mosser, B. Planetary Seismology. *Surv. . Geophys.* **14,** 239-302, http://doi.org/10.1007/BF00690946 (1993).

[15] Murdoch, N. et al.Evaluating the Wind-Induced Mechanical Noise on the InSight Seismometers. *Space Sci. Rev.*, **211,** 429-455, http://doi.org/10.1007/s11214-016-0311-y (2017).

[16] Kenda, B. et al. Modeling of ground deformation and shallow surface waves generated by Martian dust, devils and perspectives for near-surface structure inversion. *Space Sci. Rev.* **211,** 501-524, http://doi.org/10.1007/s11214-017-0378-0 (2017).

[17] Murdoch, N. et al. Estimations of the seismic pressure noise on Mars determined from Large Eddy Simulations and demonstration of pressure decorrelation techniques for the InSight mission. *Space Sci. Rev.* **211** 457-483, http://doi.org/10.1007/s11214-017-0343-y (2017).

[18] Murdoch, N. et al. Flexible Mode Modelling of the InSight Lander and Consequences for the SEIS Instrument. *Space Sci. Rev*. **214,** 117 http://doi.org/10.1007/s11214-018-0553-y (2019).

[19] Mimoun, D. et al. The Noise Model of the SEIS Seismometer of the InSight Mission to Mars. *Space Sci. Rev.* **211,** 383–428, https://doi.org/10.1007/s11214- 017-0409-x (2017).

[20] Fayon, L.et al. A Numerical Model of the SEIS Leveling System Transfer Matrix and Resonances: Application to SEIS Rotational Seismology and Dynamic Ground Interaction *Space Sci. Rev.* **214,** 119, http://doi.org/10.1007/s11214-018-0555-9 (2018).

[21] Spohn, T. et al. The heat flow and physical properties package (HP^3) for the InSight mission. *Space Sci. Rev.* **214,** 96, https://doi.org/10.1007/s11214-018-0531-4 (2018).

[22] Kedar, S.et al., Analysis of Regolith Properties Using Seismic Signals Generated by InSight's HP3 Penetrator. *Space Sci. Rev.* **211,** 315, https://doi.org/10.1007/s11214-017-0391-3 (2017).

[23] Brinkman, N et al. The first active seismic experiment on Mars to characterize the shallow subsurface structure at the InSight landing site. *SEG Technical Program Expanded Abstracts*, 4756-4760, https://doi.org/ 10.1190/segam2019-3215661.1 (2019).

[24] Sorrells, G.G. A Preliminary Investigation into the Relationship between Long-Period Seismic Noise and Local Fluctuations in the Atmospheric Pressure Field. *Geophys. J. Int*., **26,** 71-82, https://doi.org/10.1111/j.1365-246X.1971.tb03383.x (1971).

[25] Lorenz, R. D. et al. Seismometer Detection of Dust Devil Vortices by Ground Tilt. *Bull. Seism. Soc. .Am.* **105,** 3015-3023, https://doi.org/10.1785/0120150133 (2015).

[26] Morgan, P. et al. A Pre-Landing Assessment of Regolith Properties at the InSight Landing Site. *Space Sci. Rev.* **214**, 104 http://doi.org/10.1007/s11214-018-0537-y (2018).

[27] Delage, P., et al. An investigation of the mechanical properties of some Martian regolith simulants with respect to the surface properties at the InSight mission landing site, *Space Sci. Rev*. **211,** 191–213, http://doi.org/10.1007/s11214-017-0339-7 (2017).

[28] InSight Marsquake Service (2020). Mars Seismic Catalogue, InSight Mission; V1 2/1/2020. ETHZ, IPGP, JPL, ICL, ISAE-Supaero, MPS, Univ Bristol. Dataset. http://doi.org/10.12686/a6

[29] Dainty, A. M. et al. Seismic scattering and shallow structure of the moon in oceanus procellarum. *Moon* **9,** 11-29, https://doi.org/10.1007/BF00565388 (1974).

[30] Margerin, L., Campillo, M., Van Tiggelen, B., & Hennino, R. Energy partition of seismic coda waves in layered media: Theory and application to Pinyon Flats observatory. *Geophys. J. Int*. **177,** 571–585, https://doi.org/10.1111/j.1365-246X.2008.04068.x (2009).

[31] Margerin, L., Campillo, M., Shapiro, N., & van Tiggelen, B. A. Residence time of diffuse waves in the crust as a physical interpretation of coda Q: application to seismograms recorded in Mexico. *Geophys. J. Int*. **138,** 343- 352, https://doi.org/10.1046/j.1365-246X.1999.00897.x (1999).

[32] Romanowicz, B.A, Mitchell, B. J. 1.25 - Deep Earth Structure: Q of the Earth from Crust to Core, Editor(s): Gerald Schubert, *Treatise on Geophysics* (Second Edition), 789-827, (Elsevier, 2015) https://doi.org/10.1016/B978-0-444-53802-4.00021-X

[33] Gillet, K., Margerin, L., Calvet, M., & Monnereau, M.Scattering attenuation profile of the moon: Implications for shallow moonquakes and the structure of the megaregolith. *Phys. Earth Planet. Int.* **262,** 28–40, https://doi.org/10.1016/j.pepi.2016.11.001 (2017).

[34] Langston, C.A. Structure under Mount Rainier, Washington, inferred from teleseismic body waves. *J. Geophys. Res*. **84,** 4749–4762, https://doi.org/10.1029/JB084iB09p04749 (1979).

[35] Abt, D. L. et al. North American lithospheric discontinuity structure imaged by Ps and Sp receiver functions. *J. Geophys. Res.* **115,** B09301, https://doi.org/10.1029/2009JB006914 (2010).

[36] Vinnik L., Chenet, H., Gagnepain-Beyneix, J. & Lognonné, P. First seismic receiver functions on the Moon. *Geophys. Res. Lett*. **28,** 3031-3034, https://doi.org/10.1029/2001GL012859 (2001).

[37] Lognonné , P., Gagnepain-Beyneix, J. & Chenet, H. A new seismic model of the Moon: implication in terms of structure, formation and evolution. *Earth Plan. Sci. Let.* **112,** 27-44, https://doi.org/10.1016/S0012-821X(03)00172-9 (2003).

[38] Knapmeyer-Endrun, B., Ceylan, S. & van Driel, M. Crustal S-wave velocity from apparent incidence angles: a case study in preparation of InSight. *Space Sci. Rev.* **214,** 83, https://doi.org/10.1007/s11214-018-0510-9 (2018).

[39] Kolb, J. & Lekic, V. Receiver function deconvolution using transdimensional hierarchical Bayesian inference. *Geophys. J. Int.* **197,** 1719-1735, https://doi.org/10.1093/gji/ggu079 (2014).

[40] Knapmeyer, M. TTBox: A MatLab toolbox for the computation of 1D teleseismic travel times. *Seismol. Res. Lett.* **75,** 726-733, https://doi.org/10.1785/gssrl.75.6.726 (2004).

[41] Panning, M.P. et al. Planned products of the Mars Structure Service for the InSight mission, Mars. *Space Sci. Rev.* **211,** 611–650, https://doi.org/10.1007/s11214-016-0317-5 (2017).

[42] Smith, D. E. et al. Mars Orbiter laser altimeter: Experiment summary after the first year of global mapping of Mars. *J. Geophys. Res.* **106,** 23689– 23722, https://doi.org/10.1029/2000JE001364 (2001).

[43] Panning, M.P, et al. Verifying single-station seismic approaches using Earth-based data: Preparation for data return from the InSight mission to Mars. *Icarus* **248,** 230-242, https://doi.org/10.1016/j.icarus.2014.10.035 (2015).

[44] Khan, A., M. et al. , Single-station and single-event marsquake location and inversion for structure using synthetic Martian waveforms, *Physics of the Earth and Planetary Interiors*, **258**, 28-42, https://doi.org/10.1016/j.pepi.2016.05.017 (2016).

[45] Daubar, I. et al. Impact-Seismic Investigations of the InSight Mission. *Space Sci. Rev*. **214,** 132, http://doi.org/10.1007/s11214-018-0562-x (2018).

[46] Baratoux, D., Toplis, M.J., Monnereau, M. & Gasnault, O. Thermal history of Mars inferred from orbital geochemistry of volcanic provinces. *Nature* **472,** 338-341, https:/doi.org/10.1038/nature09903 (2011).

[47] Golombek, M. et al. Selection of the InSight Landing Site. *Space Sci. Rev.* **211,** 5-95, https://doi.org/10.1007/s11214-016-0321-9 (2017).

[48] Smrekar, S.E. et al. Pre-mission InSights on the Interior of Mars. *Space Sci. Rev.* **215,** 3, https://doi.org/10.1007/s11214-018-0563-9 (2019).

[49] Tittmann, B. R., Clark, V. A., Richardson, J. M., & Spencer, T. W. Possible mechanism for seismic attenuation in rocks containing small amounts of volatiles. *J. Geophys. Res.* **85,** 5199– 5208, https://doi.org/10.1029/JB085iB10p05199 (1980).

[50] InSight Mars SEIS data Service. SEIS raw data, InSight Mission. IPGP, JPL, CNES, ETHZ, ICL, MPS, ISAE-Supaero, LPG, MSFC. Other/Seismic Network, https://doi.org/10.18715/SEIS.INSIGHT.XB_2016 (2019).

Corresponding author:

Philippe Lognonné (email : lognonne@ipgp.fr)
Université de Paris-Institut de physique du globe de Paris
Equipe Planétologie et Sciences Spatiales
Université Paris Diderot
35 rue Hélène Brion
F-75013 PARIS
FRANCE

Acknowledgements:

We acknowledge NASA, CNES, their partner agencies and Institutions (UKSA, SSO, DLR, JPL, IPGP-CNRS, ETHZ, IC, MPS-MPG) and the flight operations team at JPL, SISMOC, MSDS, IRIS-DMC and PDS for providing SEED SEIS data.
The French Team acknowledge the French Space Agency CNES which has supported and funded all SEIS related contracts and CNES employees as well as CNRS and the French team universities for personal and infrastructure supports. SEIS-VBB test and development have been also supported by SESAME Ile de France in the frame of the "Centre de simulation Martien I-07-603' and 'Pole Terre Planètes 11015893'. Additional support was provided by ANR (ANR-14-CE36-0012-02, ANR-19-CE31-0008-08 for SEIS science support and ANR-11-EQPX-0040 for RESIF data access) and for IPGP team by UnivEarthS Labex program (ANR-10-LABX-0023), IDEX Sorbonne Paris Cité (ANR-11-IDEX-0005-0). Regolith stratigraphy inversion used HPC resources of CINES under the allocation A0050407341 attributed by GENCI (Grand Equipement National de Calcul Intensif).
SEIS development has been supported by SESAME Ile de France in the frame of the "Centre de simulation Martien I-07-603' and 'Pole Terre Planètes 11015893'.
Research described in this paper was partially done by the InSight Project, Jet Propulsion Laboratory, California Institute of Technology, under a contract with the National Aeronautics and Space Administration. Additional work was supported by NASA's InSight Participating Scientist Program.
The Swiss co-authors were jointly funded by (1) Swiss National Science Foundation and French Agence Nationale de la Recherche (SNF-ANR project 157133 "Seismology on Mars"), (2) Swiss State Secretariat for Education, Research and Innovation (SEFRI project "MarsQuake Service—Preparatory Phase") and (3) ETH Research grant ETH-06 17-02. Additional support came from the Swiss National Supercomputing Centre (CSCS) under project ID s992. The Swiss contribution in implementation of the SEIS electronics was made possible through funding from the federal Swiss Space Office (SSO), the contractual and technical support of the ESA-PRODEX office.
SEIS-SP development and delivery were funded by the UK Space Agency.
The SEIS leveling system development and operation support at MPS was funded by the DLR German Space Agency.

B.Tauzin and L.Pan acknowledge funding from European Union's Horizon 2020 research and innovation program under the Marie Sklodowska-Curie grant under agreement No. 793824 and 751164. The authors acknowledge three anonymous reviewers for their constructive review.
This paper is InSight Contribution Number 101 and IPGP contribution 4099.

Author Contributions:

P.Lo. leads the SEIS experiment and the VBB sensors. He designed the higher levels requirements of the experiment together with D.M. He led the manuscript team effort, contributed to several supplements and integrated all contributions. W.B.B. leads the InSight mission and US contribution to SEIS. W.T.P., D.G. and U.C. lead the SP, Ebox and LVL respectively. W.T.P. contributed to several supplements. D.B., J.A.R.M., C.T.R. lead the APSS, TWINS and IFG instruments.
E.B. contributes to the SEIS operation at JPL, together with C.Y. at CNES. M.B. for the LVL, S.C., for the SP, D.M. and P.Z. for the Ebox, K.H. for the tether-shielding and S.de R., T.N., O. R., S.T. for the VBB, contributed to the SEIS subsystems and the SEIS Mars deployment and commissioning. L.K., G.P., P.La and A.S-B. contributed to the SEIS overall management and SEIS Mars deployment and commissioning. J.C., M.B., C.C., S.C., M. van D., A.H., A.K., T.K., G.M., J.R.S., S. St., contribute to the MQS frontline activity and D.G., W.B.B., P.Lo, D.B., R.F.G., D.G., S. K., M.P., W.T.P., S. Sm, A.S., R. W. to the MQS review. E. B., F. E., C.P., S.St. contribute to the MQS and ERP operations. N.C., C.J., contributed to the SEIS analysis and Mars deployment. C.B., E.B., I.D., M.G., J.I., A.C.P., R.L., J.T. reviewed the manuscript. All authors read and commented the manuscript.

W.T.P. and P.Lo. led the analysis of supplement 1. C.C., R.F.G., A.E.S., J.B.MacC., C.P., S. B. and L.P. analyzed the data. D.M. provided the environmental noise model. S.C. provided the seismic event catalog data. E.S. and M.S. provided the polarization analysis. L.P. provided the VBB-POS outputs analysis. A.S. and D.B. provided the environmental data.

P.Lo. and S.K. led the analysis of supplement 2. L.F. developed the LVL inversion methodology with support of P.Lo.. P.D. and P.Lo. discussed the results and P.D. provided additional laboratory experiment support. L.F. and M van D. performed the resonances analysis. T.S. leads the HP3 experiment and contributed to the execution of the HP3-SEIS experiment and the interpretation of the results. D.S. and F.A. implemented in collaboration with C.S. and J.R. the aliased-data reconstruction algorithm developed by D.S., F.A. and J.R.. N.B., J. ten P., and C.S. implemented the clock time processing in collaboration with D.S.. N.B., C.S., D.S. and M. van D. processed and interpreted the travel time data in collaboration with J.R.. C.S. and M. van D. contributed to the writing of the main text section related to subsurface, and N.B., D.S., C.S. and M. van D. in collaboration with J.R. and F.A. wrote Supplement 2. A.H. contributed to the HP3-SEIS analysis. S.K., J.K., C.K., L.R., J.V., N.V. developed the timing tools between the lander, HP3 and SEIS. B.K. and N.M. developed the modeling and inversion tools for dust devils, processed the corresponding data and wrote the Supplement II-3. C.P. and S.R. developed the automatic HiRise dustdevil track software. M.D. developed the subsurface inversion tool with contributions of B.K. and P.Lo. and write the supplement II-4. All discussed the overall results. N.T. and C.V. contributed to the discussion on regolith and duricrust properties.

Supplement 3 was written and led by L.M., T.K. and N.S.. The scattering and attenuation scenarios for the Sol 128 and Sol 173 events were developed by T.K., P.Lo.. and L.M. R.F.G. provided deglitched waveforms. E.S., M.S. and E.B. analyzed the polarization and incidence angle of the Sol 173 event. Diffusion calculations were performed by W.T.P., N.S., L.M., P.Lo. and M.P.. Radiative transfer models were developed by L.M.. M.C. and S.M. compiled the measurements and waveforms pertaining to Fig. S3-12. The results were interpreted by P.Lo., T.K. and L.M.. Reviews were provided by C.B., T. N-M., A. P. and R.W..

B.K-E., B.T. and M.P. coordinated the receiver function study in supplement 4. B.K-E. (Method D), V.L. (Method A), B.T. (Method B), S.T. (Method C), A.K. and F.B. (Method E) calculated receiver functions using various methods, discussed the results, contributed to the interpretation, and drafted the manuscript. R.J. performed the inversion of S0173a data. B.K-E. and B.T. calculated synthetic receiver functions. M.P. contributed to the interpretation and participated in discussions and writing. P.D., P.Lo., B.P. and R.F.G., and J.-R.S. contributed deglitched waveforms for S0173a. S.St. provided the probability distribution of ray parameters for S0173a. M.K. produced the schematic diagrams in Fig. 6 and participated in discussions. The elastic properties compilation was provided by C.P., L.P., D.A., A.J., C.M., M.G., A.K., N.F. and C. Q-N. C.B. and J.I. reviewed this supplementary material.

J.-R.S. coordinated the supplement 5 with P.D. and R.W-S. F.N. and P.Lo. led the glitch-focussed working group. P.D., P.Lo., L.P., B.P. and R.F.G. developed the glitch-removal algorithm based on the instrument transfer function. S.B., P.Lo. and E.S. developed the glitch-removal algorithm based on the deep scattering tool. J.-R.S. developed the glitch-removal algorithm based on the discrete wavelet transform. All authors analyzed the glitches, discussed the removal strategies, and approved of the manuscript.

Competing interests:

The authors declare no competing interests.

Method:

Details on methods related to the SEIS raw data analysis are given in the **Supplement materials**. This section describes in more details the inversion method used in the **Supplement 2** and **Supplement 4** for shallow layer structure inversions.

Subsurface analysis and ***Supplement 2***

A Markov chain Monte Carlo (McMC) algorithm is used to sample solutions (i.e., physical configurations) of the inverse problem that both fit the observations within errors and satisfy known (or assumed) physical *a priori* constraints. We employ a Bayesian probabilistic procedure developed[51] and tested for pre-launch works[41,43,45].

Bayesian approaches[52] allow to go beyond the classical computation of the unique best-fitting model by providing a quantitative probabilistic measure of the model resolution, uncertainties and non-unicity. One important advantage of this method is the complete independence from the choice of the starting model. To estimate the posterior distribution of the parameters, we employ the Metropolis-Hastings algorithm[53,54], which samples the model space with a sampling density proportional to the unknown posterior probability density function. Using a large amount of iterations, the samples provide a good approximation of the posterior distribution for the model parameters.

The algorithm used in the paper is divided into 4 steps:
1) The models parameters (the Young modulus and the Poisson's ratio) are randomly sampled in the parameter space. The model is divided into two parts: the regolith and the bedrock. The Young modulus and the Poisson's ratio at the surface are randomly sampled during the inversion. Equations 1 and 20 from [26] are then used to compute the whole Young modulus and Poisson's ratio profile as a function of depth within the regolith layer. The depth of the regolith/bedrock interface is randomly sampled between the surface and 20 m. The bedrock is supposed to be made of one layer.
2) Forward problem computation. The compliance as a function of frequency is calculated in the case of a horizontally layered half space[24]. The solution to the elastostatic equation is obtained with a Thomson-Haskell propagator method[55].
3) Computation of the misfit, which determines the difference between the observed data and the computed synthetic data. The input compliance as a function of frequency data is provided in the form of a 2-D matrix, which gives a weight to each (frequency, compliance) couple. In practice, each time a new model is randomly sampled, a weight is given for each frequency according to compliance value in the 2D matrix. The sum of the weights for all the frequencies gives the misfit value.
4) The current model is accepted or rejected, using the Metropolis-Hastings algorithm[53,54]. This algorithm relies on a randomized decision rule which accepts or rejects the proposed model according to its fit to the data and the prior.
5) A new model is proposed by randomly perturbing the previously accepted model. Here, the sampling of the parameter space is performed using a Gaussian function centered on the last accepted value of the parameters.

Receiver function analysis and ***Supplement 4***

Five different groups calculated RFs to compare the results of different techniques, specifically of different deconvolution methods. One of the applied methods is probabilistic and produces an ensemble of RFs. For this method, upgoing P and SV waveforms were obtained from the Z and R waveforms by applying a free-surface transfer matrix[56]. As this matrix depends on the ray parameter as well as near-surface P- and S-wave velocities, these velocities were estimated by minimizing the energy on the SV component during the first 2 seconds of the P-wave arrival[35]. The deconvolution itself was performed by applying the trans-dimensional hierarchical Bayesian deconvolution method[39]. The method uses a reversible jump Markov Chain Monte Carlo algorithm to sample one million random realizations of RFs, represented by Gaussian pulses of unknown width, lag-time, and amplitude. The number of these pulses in the RFs is also an unknown that is determined during the sampling process.
The other four groups worked with deterministic methods. To produce the RFs shown in Figure 6, two groups applied iterative time-domain deconvolution[57]. The code for this method is available

at http://eqseis.geosc.psu.edu/cammon/HTML/RftnDocs/thecodes01.html. Details on parameters used are given in ***Supplement 4***. One group applied spectral whitening and cross-correlation[58]. The parameters used in the processing and comparison of results to other methods are detailed in ***Supplement 4***. The final group calculated RFs by using a time-domain Wiener filter that transforms the complex P-wavetrain on the Z component into a band-limited spike[59,60] This Wiener filter was applied to all three components of the seismogram to produce the RFs. The processing was implemented in Seismic Handler (http://www.seismic-handler.org/) by using the *spiking* and *fold* commands. Results are compared for different parameter settings in ***Supplement 4***.

Inversion of receiver functions and apparent S-wave velocities (***Figure S4-9***) was performed using the Neighbourhood Algorithm as implemented in *dinver*[61] (www.geopsy.org). The forward computation of the receiver function waveforms in the inversion as well as those shown in ***Figure S4-6*** uses the FORTRAN code by T.Shibutani[62] contained in the original Neighbourhood Algorithm implementation by M.Sambridge[63] (http://rses.anu.edu.au/~malcolm/na/na.html).

Data availability:

All InSight SEIS data[50] used in this paper are available from the IPGP Datacenter, IRIS-DMC and NASA PDS; all InSight APSS data are available from NASA PDS (https://pds-geosciences.wustl.edu/missions/insight/index.htm).

The data used for Figure 2 have been obtained from IRIS/DMC for BFO[63] and from IPGP Data center for Lunar data (Code XA, http://datacenter.ipgp.fr/data.php).

The data displayed in Figure 5 correspond to the following events: A is a broadband (1-10Hz) moonquake waveform recorded on March 23, 1973, at Apollo Station 15; the inferred hypocenter is lat. 84°, lon. -134°, depth 58 km. B are S0128 and S0173 events described in the main text. C is a broadband (1-10Hz) regional crustal earthquake waveform recorded on April 28, 2016, at the broadband station ATE; the hypocenter is lat. 46.044°, lon. -1.037°, depth 15 km (http://doi.org/10.15778/RESIF.FR). D is a broadband (1-10Hz) waveform recorded on February 22, 2000, at Mount St. Helens station ESD[64] (now EDM); the hypocenter is lat. 46.147582°, lon. -122.145366°, depth=12.1km.

P and S arrival times for S0128a, S0173a and S0235b are from MQS[11] catalogue[28]. The S-P travel-time difference used in the scattering analysis is 75s, compatible with the reported[28] value of 84±28s.

Subsets for the models proposed for the subsurface and summary for the upper crust are available (Supplement Table 1 and 2 for subsurface, Supplement Table 3 for uppercrust). See in Supplement 2 and 4 respectively for more details.

Code availability:

See in Method section for public available codes and for associated algorithms. The multiple scattering simulation codes used in supplement 3 are available upon request to L. Margerin. (ludovic.margerin@irap.omp.eu)

Additionnal References:

[51] Drilleau, M. et al., A Bayesian approach to infer radial models of temperature and anisotropy in the transition zone from surface wave dispersion curves. *Geophy. J. Int.*, **195**, 1165-1183. https://doi.org/10.1093/GJI/GGT284 (2013).

[52] Mosegaard, K., A. Tarantola, Monte Carlo sampling of solutions to inverse problems. *J. Geophys. Res.*, **1001**, 12431-12448, http://doi.org/10.1029/94JB03097 (1995).

[53] Metropolis, N. et al. Equation of state calculations by fast computing machines. *J. Chem. Phys*., **21**, 1087–1091. https://doi.org/10.1063/1.1699114 (1953).

[54] Hastings, W. K. Monte carlo sampling methods using Markov chains and their applications. *Biometrika*, **57**, 97–109 https://doi.org/10.2307/2334940 (1970).

[55] Sorrells, G. G., McDonald, J. A., Der, Z. A., & Herrin, E. Earth Motion Caused by Local Atmospheric Pressure Changes. *Geophys. J. Int.*, **26**, 83-98. https://doi.org/10.1111/j.1365-246X.1971.tb03384.x (1971)

[56] Kennett, B. L. N. The removal of free surface interactions from three-component seismograms. *Geophys. J. Int.* **104,** 53-163 https://doi.org/10.1111/j.1365-246X.1991.tb02501.x (1991).

[57] Ligorria, J. P. & Ammon, C. J. Iterative deconvolution and receiver-function estimation. *Bull. Seism. Soc. Am.* **89,** 1395-1400 (1999).

[58] Tauzin, B., Phạm, T. S. & Tkalčić, H. Receiver functions from seismic interferometry: a practical guide. *Geophys. J. Int.* **217,** https://doi.org/10.1093/gji/ggz002 1-24 (2019).

[59] Kind, R., Kosarev, G. L. & Petersen, N. V. Receiver functions at the stations of the German Regional Seismic Network (GRSN). *Geophys. J. Int.* **121,** 191-202 https://doi.org/10.1111/j.1365-246X.1995.tb03520.x (1995).

[60] Hannemann, K., Krüger, F., Dahm, T. & Lange, D. Structure of the oceanic lithosphere and upper mantle north of the Gloria Fault in the eastern mid-Atlantic by receiver function analysis. *J. Geophys. Res.* **122,** 7927-7950 https://doi.org/10.1002/2016JB013582 (2017).

[61] Wathelet, M. An improved neighborhood algorithm: Parameter conditions and dynamic scaling. *Geophys. Res. Let.* **35,** https://doi.org/10.1029/2008GL033256 (2008).

[62] Shibutani, T., Sambridge, M. & Kennett, B. Genetic algorithm inversion for receiver functions with application to crust and uppermost mantle structure beneath eastern Australia. *Geophys. Res. Lett.* **23,** 1829-1832 https://doi.org/10.1029/96GL01671 (1996).

[63] Sambridge, M. Geophysical inversion with a neighbourhood algorithm - I. Searching a parameter space. *Geophys. J. Int.* **138,** 479-494 https://doi.org/10.1046/j.1365-246X.1999.00876.x (1999).

[64] Black Forest Observatory (BFO). Black Forest Observatory Data. GFZ Data Services. http://doi.org/10.5880/BFO (1971).

[65] University of Washington. Pacific Northwest Seismic Network. International Federation of Digital Seismograph Networks. Dataset/Seismic Network. http://doi.org/10.7914/SN/UW (1963).

Figure legends:

Figure 1: Spectrograms of the vertical, North and East components of acceleration from 0.01-50 Hz vs. Local Mean Solar Time (LMST) for typical sol 194-195. The spectrogram includes data from both the Very Broad Band (VBB) and Short Period (SP) seismometers in the bands where their respective noise is lowest: below 5 Hz, the acceleration shown is measured by the VBBs; above 5 Hz, it is measured by the SPs. 4 events associated to burst of energy in the 2.4 Hz resonances have been identified by the MarsQuake Service[12] (MQS) catalogue[28]. Data was not returned for two 12-minutes periods on one SP axis.

Figure 2: Statistical comparison of Martian, terrestrial and lunar seismic noise. The color contours show the probability density function (PDF) of Martian vertical seismic noise measured by InSight VBB and SP during Sol 194-195. It provides the fraction of time with respect to the total observation time. VBBZ and SP1 are shown for frequency <5Hz and >5Hz respectively. The red lines provide the seismic noise measured on the spacecraft's deck by the SPs. The two lines represent the 16% and 84% percentile line, which correspond to 1-sigma gaussian distribution. Gray lines are an example of terrestrial seismic noise measured at Black Forest Observatory (BFO) in Germany. STS1 data was used for long period (<2Hz) noise statistics and STS2 data was used for shorter period (>2Hz). The two lines represent the 16% and 84% percentile line. Dashed gray is the lowest noise for Earth from the Low Noise Model[10]. The white lines are an example of lunar seismic noise measured during the Apollo seismic observation. The Apollo long period seismometer was used for frequencies <1Hz and the short period seismometer was used for frequencies >1Hz. In addition to the 16% and 84% percentile line, the 2.5 % percentile curve, which correspond to the lower limit of the 2-sigma noise, is depicted in the figure to show the lowest noise level on the Moon which is most likely due to the instrument self-noise[5,11]. Finally, the black line is the theoretical instrument noise curve for the VBB estimated from noise expected from each subsystem[5]. During the night, noise levels are smaller than the minimum observed on the Moon but in both cases, these noise floors are close to those of the sensors in the 0.1-5 Hz bandwidth. The Moon is quieter than Mars during daytime due to activity in the Martian atmosphere. Note also the extreme differences between Earth, Mars and the Moon due to the lack of the oceanic micro-seism.

Figure 3: Pressure and seismic signature of two convective vortices compared to models. Data and models are filtered between 3 and 20 seconds. The three seismic components and the pressure data (black) are well modeled using the vortex model[15] (grey). The following parameters are assumed, respectively, for the short (long period events): dust devil radius of 3.5 m (6 m), core pressure drop of 11.5 Pa (14 Pa), closest approach distance of 7 m (14 m), vortex advection speeds of 4.5 m/s (2.5 m/s), Young's modulus of 200 MPa (300 MPa) and Poisson's ratio of 0.22.. The events are also well modeled using Sorrells' theory[24,16] (green) with same values for the Young's modulus. Only the vertical compliance is used for the inversion.

Figure 4: Inversion results of the regolith thickness and V_p of the underlying bedrock. We use ground compliance estimated from 360 convective vortices, and the average V_P measured in the regolith. See ***Supplement 2-4*** for methodology. A compaction-based profile[22] in the top 0.8 m is assumed. Under these conditions a relatively thin (< 2 m) regolith layer appears most likely. An inversion of the ground compliance alone, which is representative of spatially integrated properties, yields larger regolith V_p values and a thicker regolith layer (**Figure S2-5, a1-a3**).
a, The probability density function (pdf) of V_p just above the bedrock as a function of depth of the bedrock. Yellow and purple colors are low and high probability, respectively. The pdfs are computed using 12,000 models. **b**, Marginal probabilities of the regolith to bedrock transition depth. **c**, Marginal probabilities of V_p in the regolith at 0.1 m depth (light gray) and in the bedrock (dark gray). **d**, Normalized pdf showing V_p in the bedrock as a function of the depth of the regolith to bedrock transition. The normalized pdf values are computed by counting the number of models in each 20 m/s V_p interval every 0.1m depth. For a given depth, the pdf is then divided be the maximum pdf value over all the V_p intervals.

Figure 5: Comparison of seismic scattering, attenuation and seismograms on Earth, Moon and Mars. a. provides diffusivity and absorption Q_i. Except for Mars and the Moon, the scattering quality factor is given in the 1-2 Hz frequency band. To convert scattering Q_{sc} to diffusivity D we assume a shear wave velocity v_s of 3km/s and a central frequency f=1.5Hz, which yields. $Q_{sc} = \pi$ D x 1s/km^2, with D in km^2/s. The red square with uncertainties corresponds to values for S0128a, while the red squares illustrate values exploring the trade-off for S0173a and S0235b. See ***Supplement 3*** for more details. b. Several illustrative seismograms showing the impact of the geological environment on the anatomy of the seismogram for the Moon, and for Earth (crystalline Central massif, France, or Volcanic Mount St. Helens, USA). c. Mars seismograms and rays. The indicative rays of S0173a and S0128a events, made for MQS[11] catalogue[28] distances, are given for the minimum and maximum ray depth found from reference models[48]. The seismograms are the Z deglitched component, band-passed with a 4th order butterworth between 0.03-2Hz and 2Hz-7.5Hz respectively.

Figure 6: Receiver function analysis for the Martian upper crust. The schematic background diagram is showing the P-wave ray path from S0173 at 28° of epicentral distance[2,28] (green ball) to SEIS (light blue ball). The ray path was obtained by raytracing with TTBox[40] within an *a priori* Martian velocity model[41].Topography is derived from MOLA data[42] and exaggerated vertically by a factor of 8. Mountains in the background are the Elysium Montes north of InSight. ***a,*** Zoom-in on the crust below SEIS, illustrating crustal structure and the origin of the receiver-side converted phases analyzed here. The incident plane P-wave is indicated by blue rays, while the S-waves resulting from P-to-s conversion at each of the two crustal discontinuities are shown in red. Raytracing is done in a velocity model consistent with the results of the RF inversion (***Supplement 4-4***) and ***Table S4-1***, so that the two illustrated conversions correspond to the two peaks observed at 2.2-2.4 s and 4.6-4.7 s in the RFs. In addition, the ray for the direct P wave is shown. ***b,*** Various estimates of the P-to-s RFs for S0173a and S0235b, resulting from different deglitching and deconvolution methods as described in ***Supplements 4*** and ***5***. The main consistent positive arrivals as discussed in the text are marked in orange. ***c,*** RF estimates based on THB deconvolution. The blue shading indicates the probability of a certain amplitude at a certain time, with darker shades

corresponding to a higher probability. Probabilities for all four deglitching methods are combined S0173a. Red lines indicate individual average RFs, and orange bars mark main arrivals as in **b**.

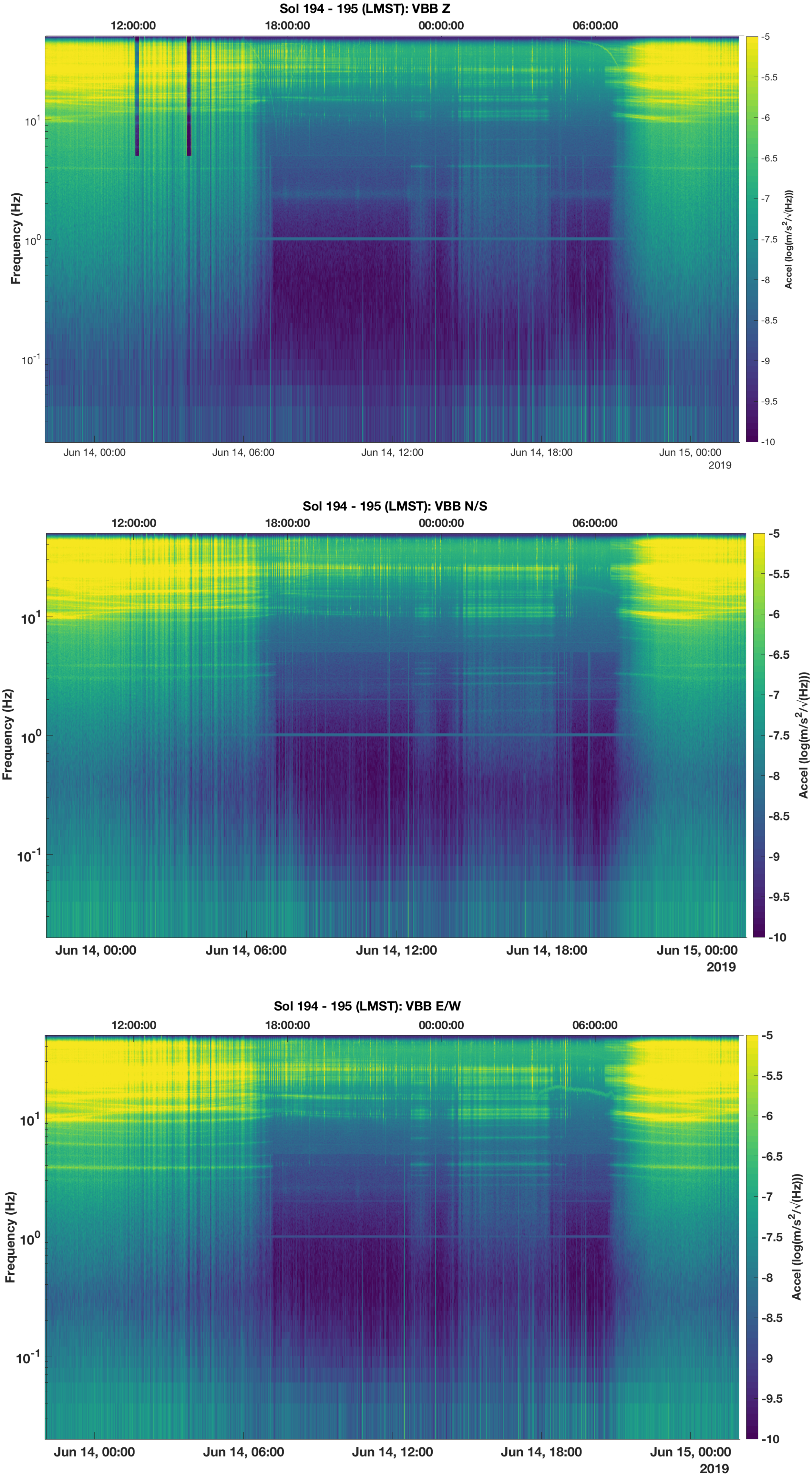
Sol 194 - 195 (LMST): VBB Z
12:00:00
18:00:00
00:00:00
06:00:00
Frequency (Hz)
10^1
10^0
10^{-1}
Jun 14, 00:00
Jun 14, 06:00
Jun 14, 12:00
Jun 14, 18:00
Jun 15, 00:00
2019
Accel (log(m/s^2/√(Hz)))
-5
-5.5
-6
-6.5
-7
-7.5
-8
-8.5
-9
-9.5
-10
Sol 194 - 195 (LMST): VBB N/S
12:00:00
18:00:00
00:00:00
06:00:00
Frequency (Hz)
10^1
10^0
10^{-1}
Jun 14, 00:00
Jun 14, 06:00
Jun 14, 12:00
Jun 14, 18:00
Jun 15, 00:00
2019
Accel (log(m/s^2/√(Hz)))
-5
-5.5
-6
-6.5
-7
-7.5
-8
-8.5
-9
-9.5
-10
Sol 194 - 195 (LMST): VBB E/W
12:00:00
18:00:00
00:00:00
06:00:00
Frequency (Hz)
10^1
10^0
10^{-1}
Jun 14, 00:00
Jun 14, 06:00
Jun 14, 12:00
Jun 14, 18:00
Jun 15, 00:00
2019
Accel (log(m/s^2/√(Hz)))
-5
-5.5
-6
-6.5
-7
-7.5
-8
-8.5
-9
-9.5
-10

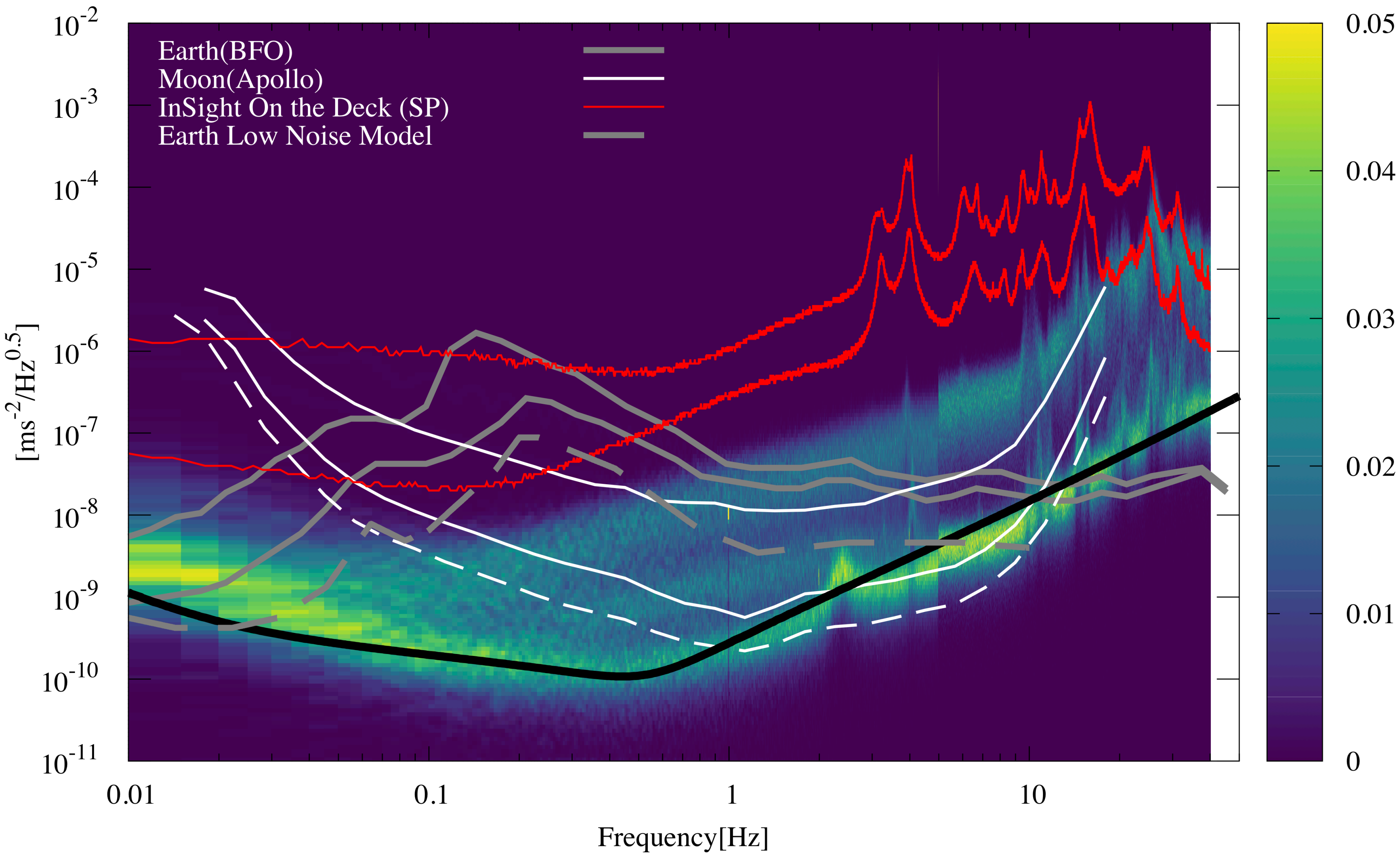
Earth(BFO)
Moon(Apollo)
InSight On the Deck (SP)
Earth Low Noise Model
10^{-2}
10^{-3}
10^{-4}
10^{-5}
10^{-6}
10^{-7}
10^{-8}
10^{-9}
10^{-10}
10^{-11}
$[ms^{-2}/Hz^{0.5}]$
0.01
0.1
1
10
Frequency[Hz]
0.05
0.04
0.03
0.02
0.01
0

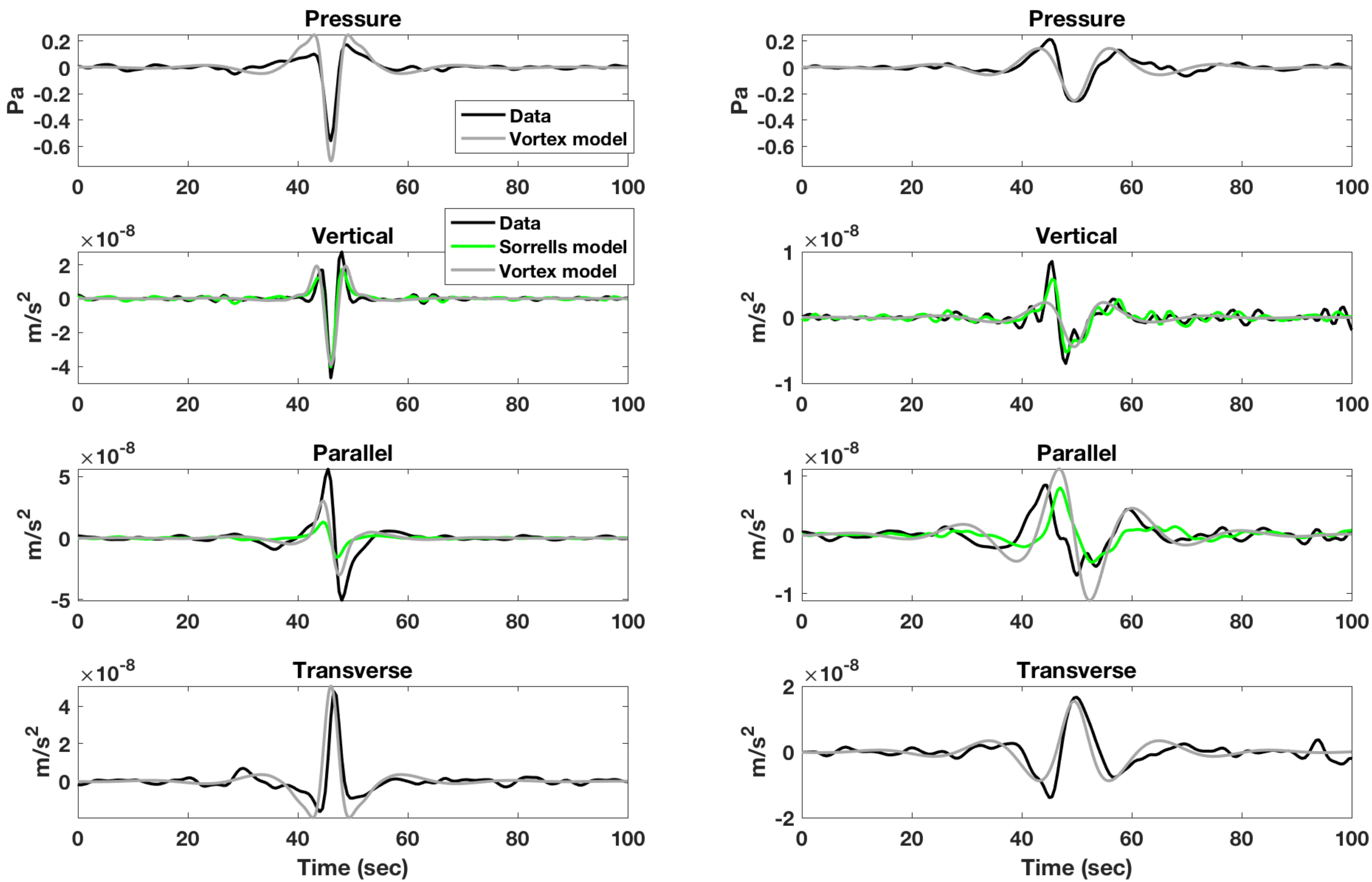

Pressure
Pa
Data
Vortex model
Time (sec)
Vertical
Parallel
Transverse
m/s^2
$\times 10^{-8}$
Sorrells model

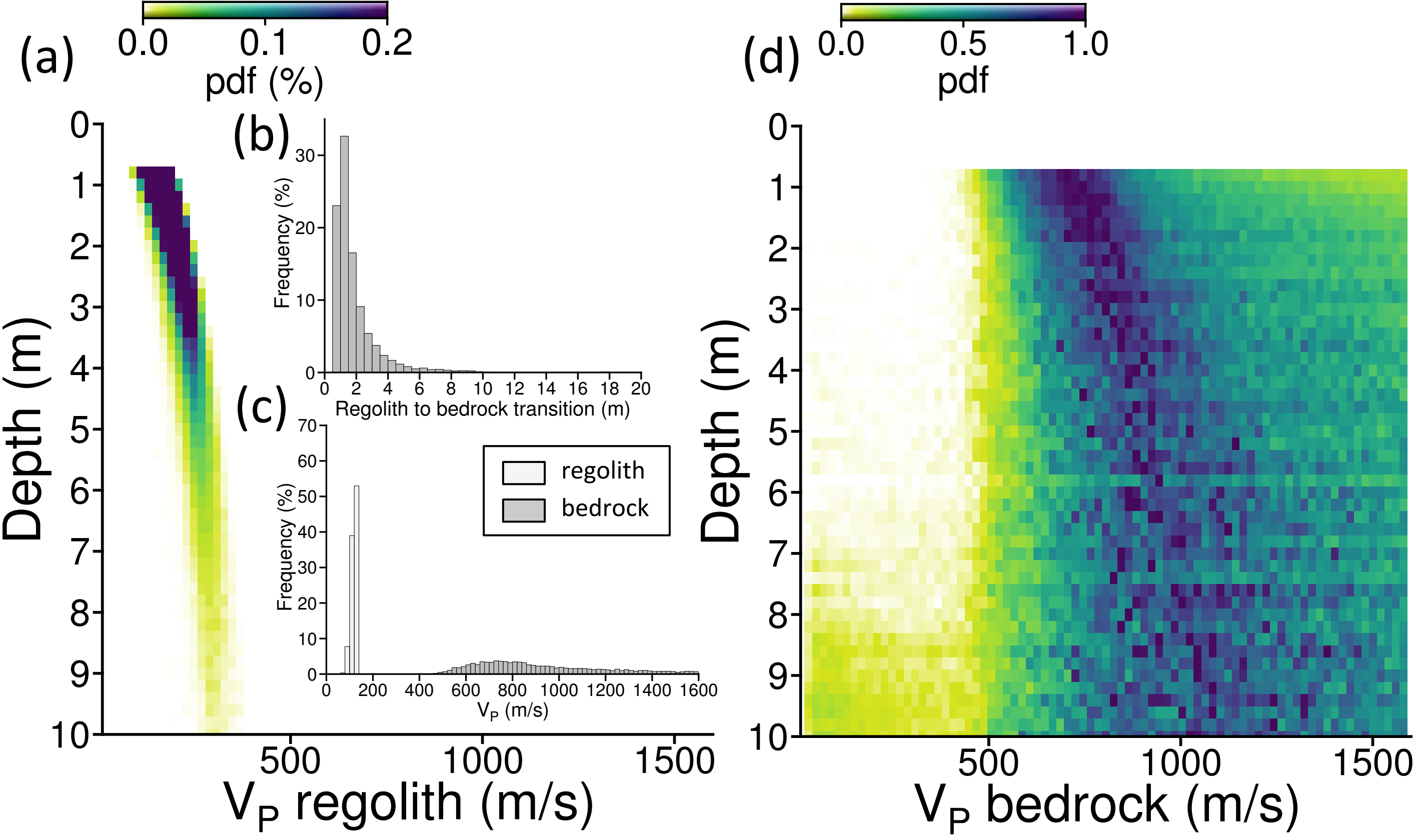

(a)
0.0
0.1
0.2
pdf (%)
Depth (m)
VP regolith (m/s)
(b)
Frequency (%)
Regolith to bedrock transition (m)
(c)
Frequency (%)
regolith
bedrock
VP (m/s)
(d)
0.0
0.5
1.0
pdf
Depth (m)
VP bedrock (m/s)

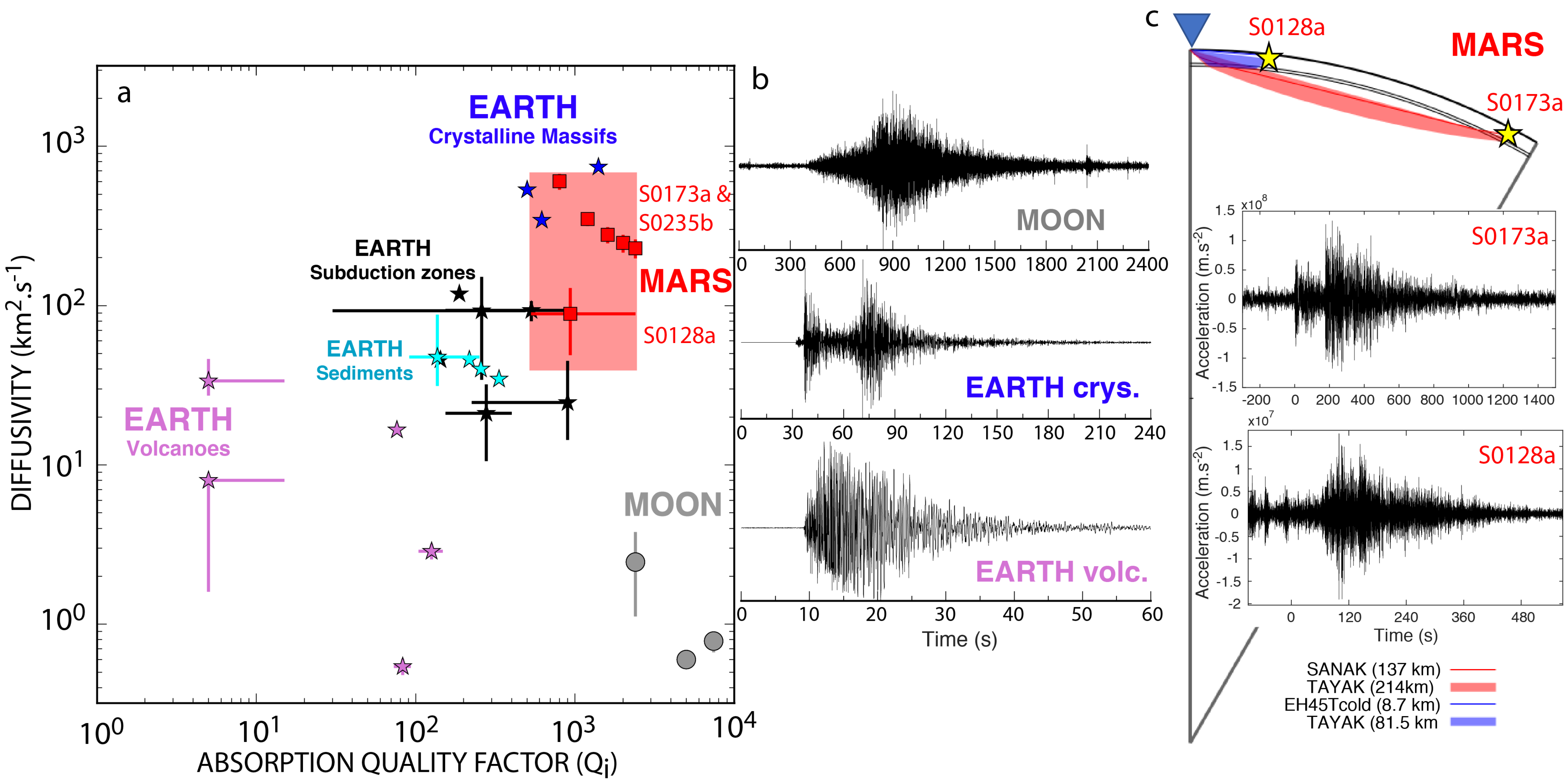

a
EARTH
Crystalline Massifs
S0173a &
S0235b
MARS
S0128a
EARTH
Subduction zones
EARTH
Sediments
EARTH
Volcanoes
MOON
DIFFUSIVITY (km^2.s^{-1})
ABSORPTION QUALITY FACTOR (Q_i)
b
MOON
EARTH crys.
EARTH volc.
Time (s)
c
MARS
S0128a
S0173a
Acceleration (m.s^{-2})
Time (s)
SANAK (137 km)
TAYAK (214km)
EH45Tcold (8.7 km)
TAYAK (81.5 km

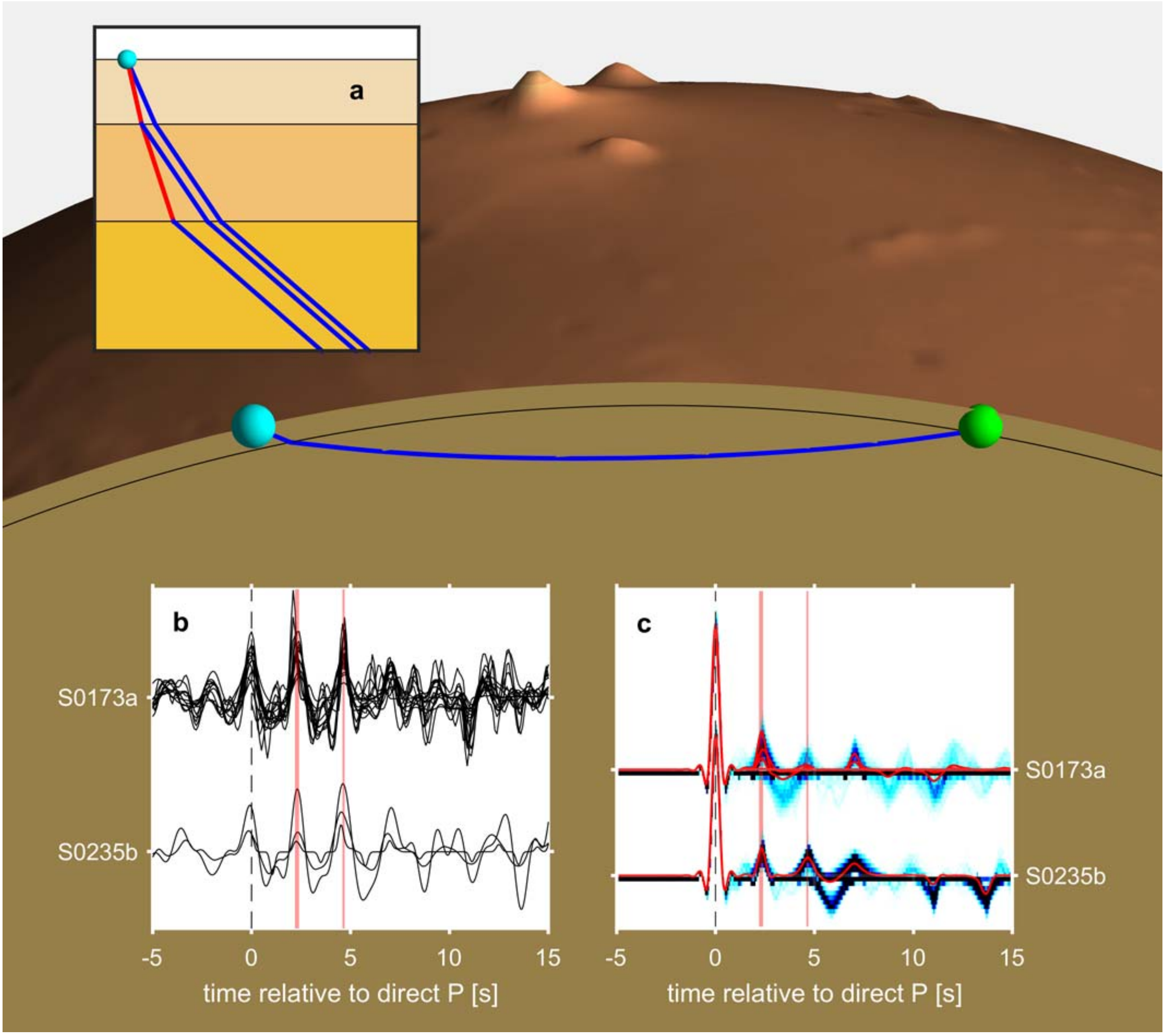
a
b
S0173a
S0235b
-5
0
5
10
15
time relative to direct P [s]
c
S0173a
S0235b
-5
0
5
10
15
time relative to direct P [s]